Structure and magnetism in Cr-embedded Co nanoparticles

Structure and magnetism in Cr-embedded Co nanoparticles

S H Baker[1], M S Kurt[1], M Roy[1], M R Lees[2] and C Binns[1]

[1] Department of Physics and Astronomy, University of Leicester, Leicester LE1 7RH, UK
[2] Department of Physics, Condensed Matter, The University of Warwick, Coventry, CV4 7AL, UK

E-mail: bak@le.ac.uk

CrossMark

Abstract

We present the results of an investigation into the atomic structure and magnetism of 2 nm diameter Co nanoparticles embedded in an antiferromagnetic Cr matrix. The nanocomposite films used in this study were prepared by co-deposition directly from the gas phase, using a gas aggregation source for the Co nanoparticles and a molecular beam epitaxy (MBE) source for the Cr matrix material. Co K and Cr K edge extended x-ray absorption fine structure (EXAFS) experiments were performed in order to investigate atomic structure in the embedded nanoparticles and matrix respectively, while magnetism was investigated by means of a vibrating sample magnetometer. The atomic structure type of the Co nanoparticles is the same as that of the Cr matrix (bcc) although with a degree of disorder. The net Co moment per atom in the Co/Cr nanocomposite films is significantly reduced from the value for bulk Co, and decreases as the proportion of Co nanoparticles in the film is decreased; for the sample with the most dilute concentration of Co nanoparticles (4.9% by volume), the net Co moment was 0.25 μ_B/atom. After field cooling to below 30 K all samples showed an exchange bias, which was largest for the most dilute sample. Both the structural and magnetic results point towards a degree of alloying at the nanoparticle/matrix interface, leading to a core/shell structure in the embedded nanoparticles consisting of an antiferromagnetic CoCr alloy shell surrounding a reduced ferromagnetic Co core.

Keywords: nanoparticles, EXAFS, magnetic moment, exchange bias

(Some figures may appear in colour only in the online journal)

1. Introduction

In recent years nanosized particles of magnetic materials, with diameters in the range 1–10 nm, have attracted much interest due to the fact that their magnetic properties differ considerably from those of the corresponding bulk material. Key reasons for the departure from bulk behaviour are the quantum size effect and the large proportion (10–50%) of atoms residing at the surface of the particle. Surface atoms are under-coordinated with respect to atoms in the interior of the nanoparticle, which leads to a narrowing of the energy bands. For transition and rare earth metals, this includes the d or f bands respectively, which govern the magnetism in these metals; this leads to size-dependent properties that are distinct from those of the bulk material. Enhancements [1–5] or reductions [2, 6] in atomic moments have been confirmed

experimentally, and in sufficiently small nanoparticles of Rh (non-magnetic in bulk form) a permanent ferromagnetic (F) moment has been observed [7].

In addition to size-related effects, a highly important factor affecting the magnetic properties of nanoparticles is their atomic structure. Atomic structure in nanoparticles can be changed pseudo-epitaxially by embedding them in a matrix of a different material, thereby potentially offering a degree of control over their magnetism. Atomic structure change has been reported in Fe and Co nanoparticles embedded in various matrices [8–21]. A convenient way of embedding nanoparticles in a matrix, directly from the gas phase, is provided by the low energy cluster beam deposition (LECBD) method [22]. This is a highly controllable technique in which nanoparticles (from a gas aggregation type source) are co-deposited with the matrix material (from a molecular beam epitaxy—MBE—source)

1

onto a solid substrate. It affords a high level of control over the atomic structure in the matrix-embedded nanoparticles. For example we have shown recently that the lattice parameter of fcc Fe nanoparticles embedded in a $Cu_{1-x}Au_x$ matrix can be controlled through control of the Au-content, and hence lattice parameter, of the $Cu_{1-x}Au_x$ matrix [20]; this led to a high level of control over the atomic moments in the fcc Fe nanoparticles, allowing optimisation to values higher than those in bulk bcc Fe, in agreement with various calculations [18, 23–25] that predict a strong dependence of fcc Fe atomic moments on lattice parameter. Optimising magnetic properties in nanocomposite materials by establishing a high degree of control over atomic structure is relevant to the drive to design new high performance magnetic materials for a variety of applications; these include the design of electric motors with improved efficiency [26], magnetic recording [27] and several biomedical applications [28, 29] which include the treatment of cancer tumours using magnetic nanoparticle hyperthermia (MNH).

There have been relatively few reports of F nanoparticles embedded in antiferromagnetic (AF) materials. Such systems are fundamentally interesting as they can act as test cases for nanoscale F–AF interfaces. It is well known that, following cooling in the presence of a magnetic field, an F–AF interface gives rise to a unidirectional anisotropy. In hysteresis measurements, this leads to the observation of a horizontal shift (exchange bias H_{ex}) in the hysteresis loop along the applied field direction; this is often accompanied by an increase in the coercivity H_c [30]. Exchange bias lies at the heart of the design of spin-valve systems; devices based on spin-valve systems include magnetoresistive read heads, MRAMs and other spintronic devices. As is known, the appearance of an exchange bias can be attributed to the pinning of magnetic moments in the F material at the F–AF interface in a single direction by the AF material. The moments in the F material can be rotated away from the pinned direction by applying an external magnetic field; it is the difference in exchange energy between parallel and antiparallel alignments of moments across the F–AF interface that gives rise to the shift or exchange bias observed in the measured hysteresis loop. (The reader is directed towards [31, 32] for reviews of this topic). More recently it has been appreciated that, in many F–AF systems, it is only a small fraction of the moments that is actually pinned [33]; the pinned fraction, and hence the values of H_{ex} and H_c, will be strongly influenced by the details of the interface microstructure. A high degree of control over sample microstructure is possible in the case of nanocomposite materials. Studying the behaviour of the F–AF interfaces in F–AF nanocomposite systems is therefore important as structural control offers the potential to tune H_{ex} and H_c.

The first experimental observation of exchange bias was reported in 1956 for partially oxidised Co particles [34]. Much of the subsequent research effort, however, was directed towards F–AF systems with thin film structures since it was recognised that the spin valve structures required in magnetic recording and sensor devices can be formed from thin film multilayer structures [35]. This was driven in part by the realisation that forming a multilayer structure of F and AF materials allows the number of F–AF interfaces to be increased. In addition, deposition techniques for thin films provide high levels of control over morphological properties such as grain size and orientation as well as overall crystalline quality, spin structure or interface layers. More recently the study of exchange bias effects in nanoparticle systems has been attracting renewed interest [36–40], since it is recognised that the exchange interaction at F–AF interfaces leads to increases in coercivity and, hence, could lead to increased magnetic hardening in permanent magnetic nanocomposites [35, 41, 42]. Increases in the thermal stability of F nanoparticle moments [43] have also been reported as a consequence of F–AF exchange. Furthermore, if the anisotropy can be controlled this could lead to the optimisation of nanoparticle performance in various applications e.g. MNH, by maximising the heat produced by the nanoparticles when subjected to an oscillating magnetic field [44]. As mentioned above, the fact that significant levels are of control are achievable over the microstructure in cluster-assembled materials should enable a degree of control over both the coercivity and exchange bias, and hence the magnetic anisotropy in nanocomposite F–AF systems. Reducing the size of both F and AF materials leads to a range of novel properties, as is known. The increasing influence of surface effects has been discussed above; reducing size can also lead to changes in the magnetization reversal modes or the appearance of superparamagnetism [45]. It is therefore important to investigate the magnetic properties in F–AF systems with a nanoscale sample structure.

In the work presented here, we report on the results of an investigation into the structure and magnetism of (F) Co nanoparticles embedded in an (AF) Cr matrix. Nanocomposite films of Cr-embedded Co nanoparticles were prepared by the LECBD technique. Atomic structure and magnetism in these samples were probed by means of extended x-ray absorption fine structure (EXAFS) and magnetometry measurements respectively. The results are discussed in the light of recent research on cluster-assembled F–AF systems [36–40]. Both the structural and magnetic measurements indicate that the Co nanoparticles alloy to a degree with the Cr matrix, leading to a core/shell structure in the embedded nanoparticles resulting in an (AF) shell of CoCr alloy surrounding a reduced (F) core of pure Co.

2. Experimental

Nanocomposite films of Cr-embedded Co nanoparticles were prepared by co-deposition under ultra-high vacuum (UHV) conditions, using a gas aggregation nanoparticle source and a Cr MBE source. The deposition rates of Co nanoparticles and Cr matrix were measured by means of a quartz crystal thickness monitor; high levels of control over these enabled a high degree of control over the volume filling fraction of embedded Co nanoparticles in the Cr matrix. A detailed description of the operation and characteristics of the gas aggregation nanoparticle source used for this work can be found elsewhere [46, 47]. The size (diameter) distribution of Co nanoparticles produced by the source during preparation of the samples used in this study is shown in figure 1. This was measured
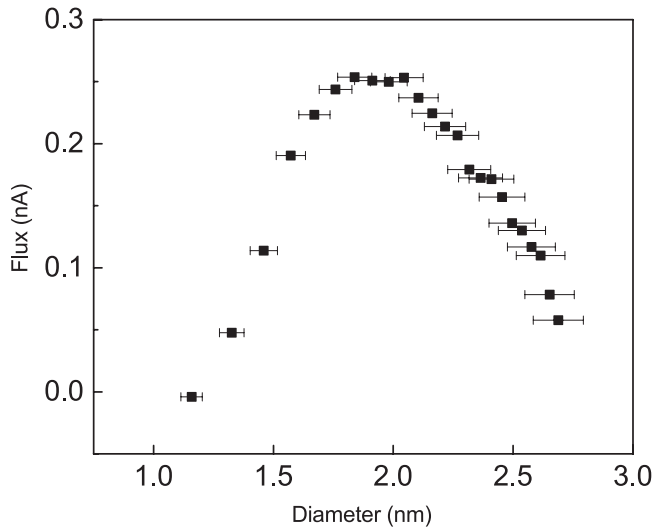
Figure 1. Size distribution of Co nanoparticles produced by the gas aggregation source during fabrication of the nanocomposite Co/Cr films.

using a quadrupole filter, mounted axially within the source. As can be seen from the figure, the mean size of Co nanoparticles was about 2 nm. All samples were deposited on to Si (1 0 0) substrates, and capped with about 500 Å of Ag in order to protect the samples against oxidation upon removal from the deposition chamber. Some CoCr atomic alloy films were also prepared, using Co and Cr MBE sources, for the purposes of comparison.

Atomic structure in the Cr-embedded Co nanoparticles was probed by means of Co K edge EXAFS measurements. Some Cr K edge EXAFS measurements were also performed in order to check the atomic structure in the Cr matrix. The experiments were performed on beam-line I18 at the Diamond Light Source. X-ray absorption spectra were recorded at room temperature in fluorescence, using a 9-element monolithic Ge detector. The energy of the incident x-rays was selected with a double crystal Si(1 1 1) monochromator, while an ionisation chamber filled with He was used to measure the incident x-ray intensity. Background-subtraction and normalisation of the measured absorption spectra was carried out using the program PySpline [48] to yield the EXAFS spectra $\chi(k)$, where k is the photoelectron wavevector. These could then be analysed to obtain structural information, by fitting the experimental $\chi(k)$ to calculated EXAFS functions. Structural parameters extracted from the data were: interatomic distances r_i, mean square variations in interatomic distance (Debye–Waller factors) σ_i^2 and coordination numbers N_i. An additional parameter E_F, which is a correction to the absorption edge energy, was also included in the analysis procedure. The fitting procedure was carried out using the EXCURV98 program [49]. This uses fast curved wave theory [50] to calculate the EXAFS; atomic scattering potentials and phase shifts are calculated using Hedin–Lundqvist potentials, which account for amplitude reduction effects in EXAFS [51]. EXCURV98 uses a least squares refinement to fit the data, and minimises the sum of the square of the residuals (with k^3 weighting) according to

$$\Phi = \sum_n \left| k^3 \chi_{\text{exp }t}(k_n) - k^3 \chi_{\text{fit}}(k_n) \right|^2 / \left(\sum_n \left| k^3 \chi_{\text{exp }t}(k_n) \right| \right)^2$$

A value of around 10 for Φ ($\times 10^4$) would normally be considered to represent a reasonable fit. We also quote the EXAFS R-factor which is widely regarded as a measure of the quality of the fit. This is defined (with k^3 weighting), according to

$$R = \sum_n \left| k^3 \chi_{\text{exp }t}(k_n) - k^3 \chi_{\text{fit}}(k_n) \right| / \left(\sum_n \left| k^3 \chi_{\text{exp }t}(k_n) \right| \right) \times 100$$

An R-value of between 20 and 30 would normally be regarded as a reasonable fit. The errors on all quantities are quoted to ± 2 standard deviations.

Magnetic properties of the Co/Cr nanocomposite films were investigated using an Oxford Instruments MagLab vibrating sample magnetometer. Magnetisation curves (total sample magnetic moment versus applied magnetic field) were recorded for temperatures in the range 2–30 K, and for fields between $\pm 4T$.

3. Structure

3.1. Cr matrix

Figure 2 shows the Cr K edge EXAFS spectra, weighted by k^3, and their associated Fourier transforms for the Cr-embedded Co nanoparticle films. Also included in the figure is data for a pure Cr MBE-deposited film. Analysis of the data for the pure Cr film yielded a fit with five statistically significant shells that was consistent with a bcc structure, as expected for bulk Cr. In the fitting procedure for this sample, the coordinations were held fixed at values associated with bcc while the interatomic distances r_i and Debye-Waller factors σ_i^2 were allowed to vary freely. Multiple scattering between the first and fifth shells, as expected in bcc structures, was incorporated in the fit. Table 1 gives the fit parameters obtained along with the interatomic distances and coordinations in bulk Cr. The Cr edge spectra for the nanocomposite films look qualitatively similar to the pure Cr spectrum. Good N_i-constrained fits, consistent with bcc, were also obtained for these samples. The fit values are listed in table 1, and indicate a bcc structure in the embedding Cr matrix. It can be noted that the fit values for σ_i^2 are larger for the 43% VF Co/Cr film than for the 7.1% VF film or the pure Cr film. This is consistent with the observation that the amplitude of the EXAFS for this sample is lower than for the other two samples (see figure 2), implying that the high concentration of Co nanoparticles in the 43% VF film results in a certain amount of disruption or disorder of the Cr matrix. [It may also be noted that the fit values for σ_i^2 appear to be a little lower in the 7.1% VF Co/Cr film than in the Cr MBE film. Obtaining sufficient equivalent thickness of Co for the Co edge EXAFS measurements necessarily results in a large Cr thickness (~0.5 μm) for films with dilute filling fraction of Co. The thickness of the Cr MBE film was much thinner than this (~10%); the influence of the surface layers in this sample will be larger than for the 7.1% VF Co/Cr film which
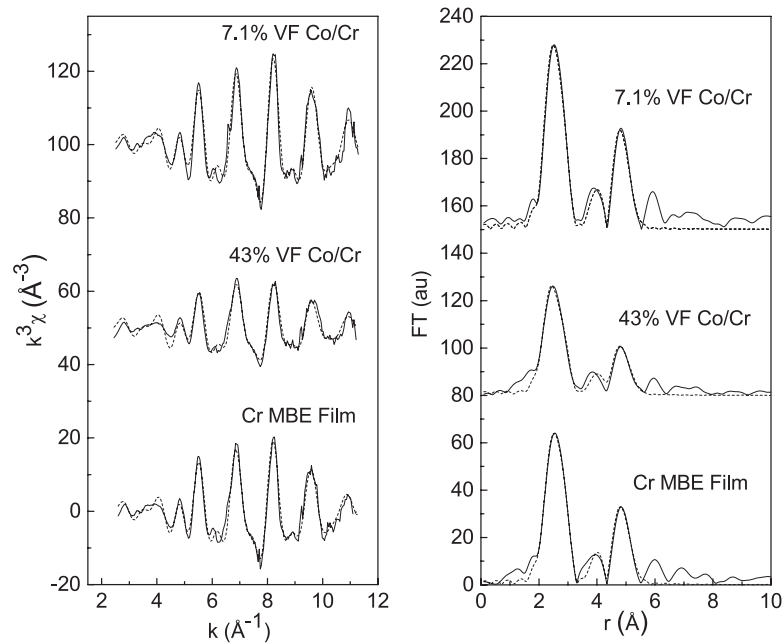
Figure 2. Cr K edge EXAFS spectra χ, weighted by k^3, and associated Fourier transforms for Cr-embedded Co nanoparticle films, and for a pure Cr film. The full line represents the data and Fourier transform of the data while the dashed line represents the fit to the data and Fourier transform of the fit. (The spectra for the 43% Co/Cr and 7.1% VF Co/Cr films have been displaced by 50 Å^{-3} and 100 Å^{-3} respectively; their Fourier transforms have been displaced by 80 au and 150 au respectively).

could be responsible for the larger values of σ_i^2 in this case. We would point out, however, that σ_1^2 for the Cr film is, within the errors involved, only slightly higher than for the 7.1% VF film; all other σ_i^2 values are, within experimental error, consistent between the two samples].

3.2. Co Nanoparticles

The Co K edge EXAFS spectra (k^3-weighted) measured for the Cr-embedded Co nanoparticle films, and associated Fourier transforms, are shown in figure 3. Data for a pure Co MBE-deposited film is also included in the figure. Analysis of the pure Co data yielded a 5-shell fit consistent with an hcp structure, as expected for bulk Co. During the fit for this sample, the coordinations were held fixed at values associated with hcp while r_i and σ_i^2 were allowed to vary freely. The fit parameters obtained, along with the interatomic distances and coordinations in bulk Co, are given in table 2.

Upon initial inspection, the Co edge spectra for the Co/Cr nanocomposite films look rather different to the pure Co spectrum. It is worth pointing out that in previous studies [19], the Co edge EXAFS measured by us for Co nanoparticles embedded in a Ag matrix appeared very similar to that for a pure Co film; data analysis confirmed the retention of a close-packed structure in this case. The differences in the Co edge EXAFS in figure 3 therefore imply a different structure in the Cr-embedded Co nanoparticles. As is known, even partial oxidation gives rise to strong changes in the Co K edge EXAFS relative to that for the pure metal [52], particularly in the low k-region. However, none of the features associated with oxidation were found in the Co K edge spectra presented here.

The spectra for the samples with the most dilute concentrations of Co nanoparticles (7.1% VF and 11.5% VF) in fact

show some similarity with the Cr edge spectra in figure 2, which hints at a bcc structure in the embedded Co nanoparticles. This is reinforced by the fact that is it is possible to obtain reasonable bcc fits (with four significant shells) to the data for these two samples. Table 3 gives the fit parameters r_i and σ_i^2 obtained in such fits (in which N_i were fixed at values associated with bcc). The fit values for r_i are in reasonable agreement with those measured previously for bcc Co nanoparticles embedded in an Fe matrix [15]. In fact, the nearest neighbour distance r_1 (at 2.47 ± 0.01 Å) is slightly larger than in the Fe-embedded Co nanoparticles of [15] (at 2.45 ± 0.01 Å); this is consistent with the fact that Co has a slightly larger lattice parameter than Fe (2.91 Å compared to 2.87 Å respectively), and is hence consistent with some stretch in the Cr-embedded Co nanoparticles relative to those embedded in Fe. We also note that the fit values for σ_i^2 in table 3 are generally larger than those found from analysis of the Cr edge EXAFS for the 7.1% VF Co/Cr film and the pure Cr film (see table 1). This is consistent with the observation that the amplitude of the bcc Co edge EXAFS for the 7.1% VF and 11.5% VF Co/Cr films (see figure 3) is lower than the amplitude of the bcc Cr edge EXAFS in the 7.1% VF Co/Cr film and pure Cr film (see figure 2). These results imply a degree of disorder in the embedded Co nanoparticles.

It is known that Co nanoparticles can undergo significant alloying when embedded in certain matrix materials, such as Mn for example [38]. Given the close similarity between the atomic numbers of Co and Cr, it is of course difficult on the basis of EXAFS alone to determine the extent of any alloying between Co nanoparticles and Cr matrix. The fit parameters in table 3 were obtained on the basis of Co scattering atoms. Replacing the Co scattering atoms by Cr atoms in the fitting procedure changes the fit parameters only very slightly.

Table 1. Structural parameters r_i, $2\sigma_i^2$ (interatomic distances and Debye–Waller factors) obtained from bcc fits to the Cr K edge EXAFS spectra measured for the Co/Cr nanocomposite films.

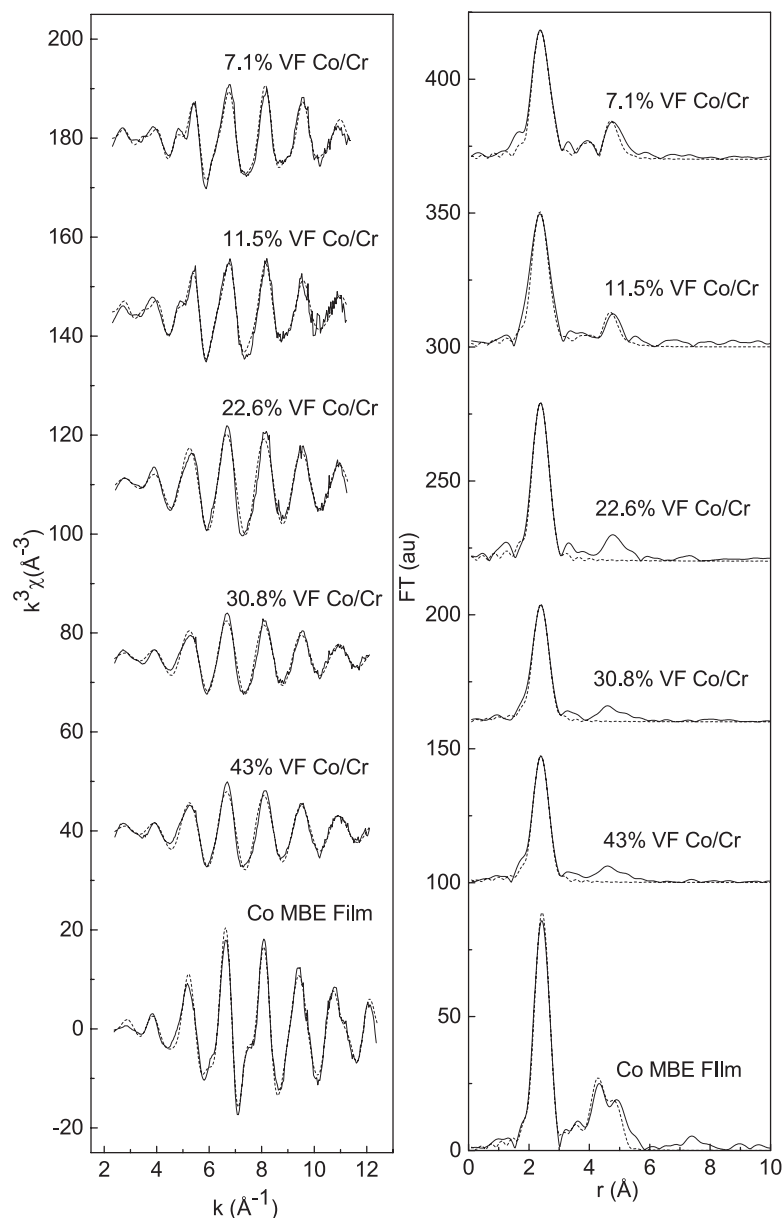|	Shell 1	Shell 2	Shell 3	Shell 4	Shell 5
bcc Cr	$r_1 = 2.52$ Å $N_1 = 8$	$r_2 = 2.91$ Å $N_2 = 6$	$r_3 = 4.12$ Å $N_3 = 12$	$r_4 = 4.83$ Å $N_4 = 24$	$r_5 = 5.04$ Å $N_5 = 8$
Cr MBE film	$r_1 = 2.51 \pm 0.01$ Å $2\sigma_1^2 = 0.019 \pm 0.002$ Å²	$r_2 = 2.87 \pm 0.02$ Å $2\sigma_2^2 = 0.015 \pm 0.002$ Å²	$r_3 = 4.10 \pm 0.02$ Å $2\sigma_3^2 = 0.030 \pm 0.005$ Å² $E_F = -12.9 \pm 0.7$ eV $\Phi \times 10^4 = 5.2$ $R = 28.6$	$r_4 = 4.80 \pm 0.03$ Å $2\sigma_4^2 = 0.024 \pm 0.004$ Å²	$r_5 = 5.02 \pm 0.04$ Å $2\sigma_5^2 = 0.029 \pm 0.007$ Å²
Film of 7.1% VF Co nanoparticles in a Cr matrix	$r_1 = 2.50 \pm 0.01$ Å $2\sigma_1^2 = 0.014 \pm 0.002$ Å²	$r_2 = 2.86 \pm 0.02$ Å $2\sigma_2^2 = 0.015 \pm 0.002$ Å²	$r_3 = 4.10 \pm 0.02$ Å $2\sigma_3^2 = 0.025 \pm 0.004$ Å² $E_F = -13.2 \pm 0.8$ eV $\Phi \times 10^4 = 5.1$ $R = 29.5$	$r_4 = 4.80 \pm 0.02$ Å $2\sigma_4^2 = 0.020 \pm 0.004$ Å²	$r_5 = 5.00 \pm 0.04$ Å $2\sigma_5^2 = 0.025 \pm 0.007$ Å²
Film of 43.0% VF Co nanoparticles in a Cr matrix	$r_1 = 2.50 \pm 0.01$ Å $2\sigma_1^2 = 0.022 \pm 0.002$ Å²	$r_2 = 2.85 \pm 0.02$ Å $2\sigma_2^2 = 0.022 \pm 0.003$ Å²	$r_3 = 4.09 \pm 0.03$ Å $2\sigma_3^2 = 0.039 \pm 0.007$ Å² $E_F = -12.9 \pm 0.8$ eV $\Phi \times 10^4 = 7.9$ $R = 35.4$	$r_4 = 4.80 \pm 0.04$ Å $2\sigma_4^2 = 0.042 \pm 0.011$ Å²	$r_5 = 4.98 \pm 0.03$ Å $2\sigma_5^2 = 0.028 \pm 0.006$ Å²

Figure 3. Co K edge EXAFS spectra χ, weighted by k^3, and associated Fourier transforms for Cr-embedded Co nanoparticle films, and a pure Co film. The full line represents the data and Fourier transform of the data while the dashed line represents the fit to the data and Fourier transform of the fit. (The spectra for the 43%, 30.8%, 22.6%, 11.5% and 7.1% VF Co/Cr films have been displaced by 40, 75, 110, 145 and 180 Å^{-3} respectively; their Fourier transforms have been displaced by 100, 160, 220, 300 and 370 arb. units respectively).

The interatomic distances increase by 0.01–0.03 Å, although in most cases the increase is within the experimental errors involved. For the 7.1% VF Co/Cr film the fit indices $\Phi \times 10^4$ and R increase slightly from 3.9 to 4.5, and from 25.0 to 27.6 respectively. Small increases in fit indices are also seen for the 11.5% VF Co/Cr film, from 4.9 to 5.5 for $\Phi \times 10^4$, and 27.9 to 31.0 for R. We note, however, that 'artificially' replacing Co scatterers with Cr scatterers in the fit to the data for the pure Co MBE film produces a much more significant worsening in fit; $\Phi \times 10^4$ and R increase respectively from 2.2 to 4.7, and from 19.3 to 29.9. This 'comparative' procedure suggests that in the 7.1% and 11.5% VF Co/Cr films, Co atoms are coordinated by both Co and Cr atoms, although slightly more by Co than Cr. As such, this is consistent with a degree of alloying between the Co nanoparticles and Cr matrix. It should be noted

that in the absence of alloying, Co atoms would on average be coordinated significantly more by Co than by Cr atoms. In a 2 nm nanoparticle, the proportion of atoms residing at the surface is ~40% [53]; in the absence of alloying, nearest neighbour partial Co–Cr and Co–Co coordinations of 1.6 and 6.4 respectively would then be expected. It should also be noted that the bcc structure has been observed in CoCr alloys for Co-contents up to 30 at.% [54]; a degree of alloying is therefore not inconsistent with the bcc structure that we have found here for the Cr-embedded Co nanoparticles.

For the Co/Cr nanocomposite films containing higher volume fractions of Co nanoparticles (22.6%, 30.8% and 43.0%), the Co edge EXAFS spectra look rather 'simpler' than the spectra discussed above for the two most dilute volume fractions (as can be seen in figure 3). In fact it is possible to fit

Table 2. Structural parameters r_i, $2\sigma_i^2$ (interatomic distances and Debye–Waller factors) obtained from hcp fit to the Co K edge EXAFS spectrum measured for a pure Co film.

	Shell 1	Shell 2	Shell 3	Shell 4	Shell 5
hcp Co	$r_1 = 2.50$ Å $N_1 = 12$	$r_2 = 3.54$ Å $N_2 = 6$	$r_3 = 4.07$ Å $N_3 = 2$	$r_4 = 4.34$ Å $N_4 = 18$	$r_5 = 4.78$ Å $N_5 = 12$
Co MBE film	$r_1 = 2.50 \pm 0.01$ Å $2\sigma_1^2 = 0.015 \pm 0.001$ Å²	$r_2 = 3.52 \pm 0.03$ Å $2\sigma_2^2 = 0.0030 \pm 0.006$ Å²	$r_3 = 4.02 \pm 0.08$ Å $2\sigma_3^2 = 0.028 \pm 0.023$ Å²	$r_4 = 4.37 \pm 0.01$ Å $2\sigma_4^2 = 0.020 \pm 0.002$ Å²	$r_5 = 4.85 \pm 0.02$ Å $2\sigma_5^2 = 0.015 \pm 0.002$ Å²

$$E_F = -12.4 \pm 0.6 \text{ eV}$$
$$\Phi \times 10^4 = 2.2$$
$$R = 19.3$$

Table 3. Structural parameters r_i, $2\sigma_i^2$ (interatomic distances and Debye–Waller factors) obtained from fits to the Co K edge EXAFS spectra measured for the 7.1% VF and 11.5% VF Co/Cr nanocomposite films.

	Shell 1	Shell 2	Shell 3	Shell 4
Film of 7.1% VF Co nanoparticles in a Cr matrix	$r_1 = 2.47 \pm 0.01$ Å $2\sigma_1^2 = 0.018 \pm 0.001$ Å^2 $N_1 = 8$	$r_2 = 2.82 \pm 0.03$ Å $2\sigma_2^2 = 0.053 \pm 0.009$ Å^2 $N_2 = 6$	$r_3 = 4.08 \pm 0.02$ Å $2\sigma_3^2 = 0.036 \pm 0.005$ Å^2 $N_3 = 12$	$r_4 = 4.76 \pm 0.01$ Å $2\sigma_4^2 = 0.029 \pm 0.003$ Å^2 $N_4 = 24$
			$E_F = -10.5 \pm 0.7$ eV $\Phi \times 10^4 = 3.9$ $R = 25.0$	
Film of 11.5% VF Co nanoparticles in a Cr matrix	$r_1 = 2.47 \pm 0.01$ Å $2\sigma_1^2 = 0.020 \pm 0.001$ Å^2 $N_1 = 8$	$r_2 = 2.81 \pm 0.06$ Å $2\sigma_2^2 = 0.075 \pm 0.020$ Å^2 $N_2 = 6$	$r_3 = 4.08 \pm 0.03$ Å $2\sigma_3^2 = 0.046 \pm 0.008$ Å^2 $N_3 = 12$	$r_4 = 4.75 \pm 0.02$ Å $2\sigma_4^2 = 0.035 \pm 0.003$ Å^2 $N_4 = 24$
			$E_F = -10.3 \pm 0.9$ eV $\Phi \times 10^4 = 4.9$ $R = 27.9$	

Table 4. Structural parameters N_i, r_i, $2\sigma_i^2$ (coordinations, interatomic distances and Debye–Waller factors) obtained from fits to the Co K edge EXAFS spectra measured for the 22.6% VF, 30.8% VF and 43.0% VF Co/Cr nanocomposite films.

	Shell 1
Film of 22.6% VF Co nanoparticles in a Cr matrix	$r_1 = 2.47 \pm 0.01$ Å $2\sigma_1^2 = 0.018 \pm 0.002$ Å^2 $N_1 = 9.2 \pm 0.8$ $E_F = -9.3 \pm 0.9$ eV $\Phi \times 10^4 = 4.2$ $R = 24.2$
Film of 30.8% VF Co nanoparticles in a Cr matrix	$r_1 = 2.48 \pm 0.01$ Å $2\sigma_1^2 = 0.019 \pm 0.002$ Å^2 $N_1 = 7.1 \pm 0.6$ $E_F = -9.9 \pm 0.8$ eV $\Phi \times 10^4 = 3.5$ $R = 24.4$
Film of 43.0% VF Co nanoparticles in a Cr matrix	$r_1 = 2.48 \pm 0.01$ Å $2\sigma_1^2 = 0.018 \pm 0.002$ Å^2 $N_1 = 7.2 \pm 0.6$ $E_F = -9.8 \pm 0.8$ eV $\Phi \times 10^4 = 3.5$ $R = 23.6$

only one significant shell to these spectra. The fit parameters obtained in single shell fits to these spectra are given table 4. It can be seen that the fit values for the interatomic distances (2.47/2.48 $\pm$ 0.01 Å) are consistent within experimental error with the nearest neighbour distances for the samples with the two most dilute volume fractions (at 2.47 $\pm$ 0.01 Å), and are closer to these than the nearest neighbour distance in the hcp Co film (2.50 $\pm$ 0.01 Å). We also note that the fit values for the coordinations are much nearer to the nearest neighbour coordination in bcc (8) than in hcp (12). For volume fractions greater than ~20% significant agglomerations of nanoparticles are expected as the 3D percolation threshold occurs at 24.88% [55]. If the agglomerated regions of Co revert to a close packed structure, the coordination number should increase with increasing volume fraction. The fact that this is not observed, and that the nearest neighbour distance remains close to the bcc value rather than increasing to the hcp value, indicates that the agglomerated regions retain a bcc structure (over the composition range investigated). We have previously used EXAFS to show that Co nanoparticles embedded in Fe retain a bcc structure for volume fractions approaching 40% [15]; for these Fe-embedded Co nanoparticles, fits to a bcc structure with four significant shells were possible for volume fractions between 0 and 40%. For the Cr-embedded Co nanoparticles, where multi-shell fits to bcc could only be applied for the most dilute volume fractions, it can also be noted that the amplitude of the Co edge EXAFS remains low across the composition range studied (compared to the bcc Cr edge EXAFS in figure 1). It is also much lower than the Co edge EXAFS amplitude measured for the Fe-embedded bcc Co nanoparticles in [15]. These results imply that, across the
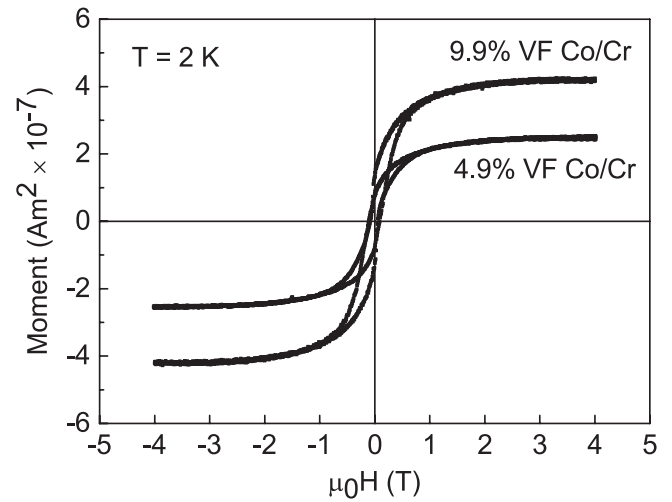

Figure 4. Magnetisation curves (total sample magnetic moment as a function of applied magnetic field) for nanocomposite Co/Cr films in which the volume fraction of Co nanoparticles is 4.9% and 9.9%. The data were recorded at a temperature of 2 K after field cooling at 0.1*T* from room temperature. (The equivalent thickness of Co and the sample area for both samples was 370 Å and 25.5 mm^2 respectively).
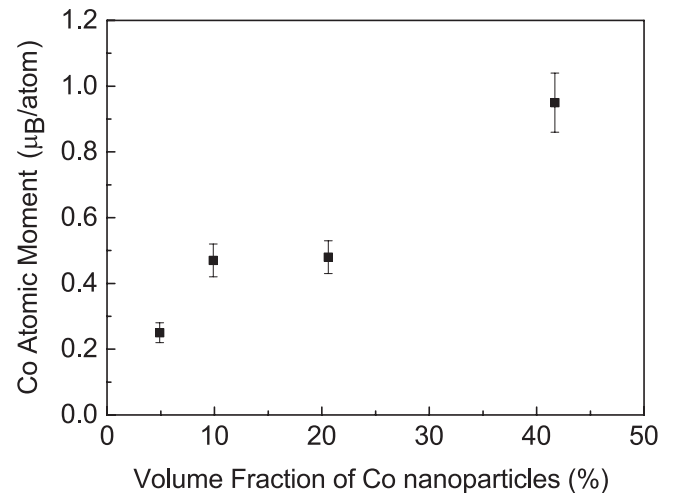

Figure 5. Net atomic Co moment in the nanocomposite Co/Cr films as a function of volume fraction of embedded Co nanoparticles.

whole composition range studied, the Cr-embedded Co nanoparticles are subject to a degree of structural disorder.

4. Magnetism

Magnetisation curves, showing the total magnetic moment in the sample as a function of applied field, are displayed in figure 4 for Co/Cr nanocomposite films with two different volume fractions of Co nanoparticles. The data was recorded at a temperature of 2 K after field cooling from room temperature at 0.1*T*. The decrease in the saturation value of the moment as the volume fraction of Co nanoparticles is reduced can be noted. With the total amount of Co in the films known, the net atomic moments on the Co atoms can be extracted from the saturation values of the sample moments. Figure 5 shows the Co atomic moments obtained in this way as a

function of volume fraction of Co nanoparticles. It is clear that not only do the Co moments decrease with decreasing volume fraction but also, that across the composition range studied, they are substantially less than the value for pure Co (1.7 μ_B/atom). For the sample with the most dilute concentration of Co nanoparticles (at 4.9% VF), the atomic Co moment is reduced to 0.25 μ_B/atom or ~15% of the bulk value. Proportionally, this reduction is appreciably greater than the reduction observed recently for the net atomic Fe moment in 2 nm Fe nanoparticles embedded in Cr [40], where the reduction was ~50% relative to the bulk Fe value. Given that ~40% of atoms in a 2 nm nanoparticle reside at its surface, a reduction in atomic moment of ~50% is consistent with the surface layer of atoms in the nanoparticle not contributing to the net atomic moment; the reduction in net Fe moment in [40] was ascribed to a magnetically disordered or AF layer of Fe atoms at the Fe/Cr interface. For the Cr-embedded Co nanoparticles here, the reduction in net moment for the 4.9% VF sample implies that ~85% of the Co atoms in the nanoparticle do not contribute to the net atomic moment which seems high in terms of a magnetically disordered or AF layer. Alternatively, as discussed below, a degree of alloying at the Co/Cr interface could account for a reduction in the net atomic Co moment (as for Co nanoparticles embedded in Mn [38]).

It is known that the saturation magnetisation, and hence the net atomic Co moment, decrease rapidly with increasing Cr content in Co-rich $Co_{1-x}Cr_x$ alloys [54, 56–58]. For $Co_{1-x}Cr_x$ alloys prepared from a melt [57] and by rf sputtering [58], the measured saturation magnetisation decreases so rapidly as the Cr content is increased that for Cr contents of ~30 at.% the samples are no longer F. In $Co_{1-x}Cr_x$ alloys formed by mechanical alloying, significant F behaviour has been observed for higher Cr contents up to approximately equiatomic compositions [54]. The decrease in saturation magnetisation has been attributed previously [54] to the dilution effect of the Co atomic moment promoted by the formation of CoCr solid solutions, and also to the competition between F and AF exchange interactions. In [57] the authors attributed the disappearance of F behaviour to AF coupling between Co and Cr atomic moments (which was consistent with neutron diffraction data [59]). As mentioned in section 2, some $Co_{1-x}Cr_x$ alloy films were prepared by MBE for comparison with the Co/Cr nanocomposite films. Figure 6 shows the magnetisation curves measured for a $Co_{0.56}Cr_{0.44}$ alloy film and also for a pure Co film. The saturation moment for the pure Co film is consistent with bulk value for the atomic Co moment, whereas the much reduced saturation moment in the alloy film yields an atomic Co moment of 0.13 ± 0.02 μ_B/atom. The same value was also obtained from the saturation moment measured for a $Co_{0.08}Cr_{0.92}$ alloy film. The observation of a small net moment in each of these two samples is consistent with an incomplete cancellation between Co and Cr moments in an otherwise AF $Co_{1-x}Cr_x$ alloy film.

For the Co/Cr nanocomposite films, a degree of alloying at the Co/Cr interface would effectively result in a core/shell structure in the embedded nanoparticles, with a $Co_{1-x}Cr_x$ alloy shell surrounding a pure Co core. Assuming such a core/shell structure, and assigning a moment of 0.13 μ_B/atom to Co atoms
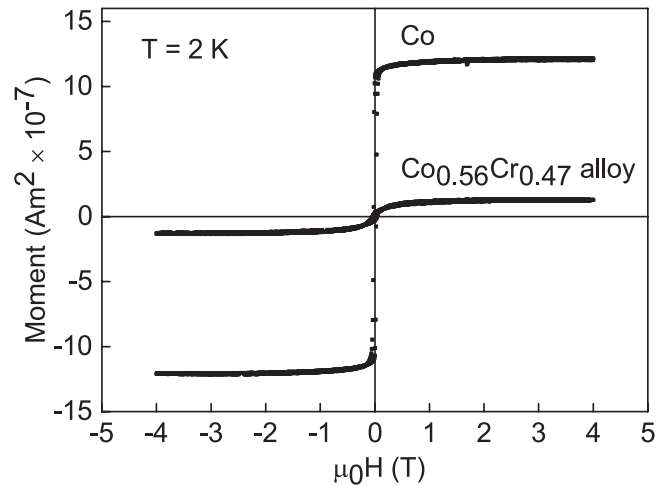

Figure 6. Magnetisation curves (total sample magnetic moment as a function of applied magnetic field) for a $Co_{0.56}Cr_{0.47}$ alloy film and a pure Co film. (The equivalent thickness of Co and the sample area for both samples was 300 Å and 25.5 mm² respectively).

in the alloy shell (as measured in the CoCr MBE alloy films) and 1.7 μ_B/atom (i.e. the bulk value) to atoms in the reduced pure Co core, the proportion of Co atoms in the nanoparticle that are alloyed can be estimated from the measured net Co moment. The figure of 0.25 μ_B/atom measured for the net Co moment in the 4.9% VF Co/Cr sample is consistent with an alloyed proportion of ~90%. This is somewhat higher than the figure of ~70% found for the alloyed proportion of Co atoms in Co nanoparticles embedded in Mn [38]. We note however that the atomic moment of Co atoms in the core is likely to be less than the bulk value, as was found for Mn-embedded Co nanoparticles [36, 37, 60] where the measured saturation magnetisation was consistent with net Co moments of ~0.1 μ_B/atom; given the degree of alloying this implies that the Co moments in the core were ~0.5 μ_B/atom. Applying this value to the atomic moments in the Co core of the Cr-embedded Co nanoparticles leads to an estimate of ~68% for the proportion of Co atoms that are alloyed. From here, it is possible to make an estimate for the nearest neighbour partial Co–Co and Co–Cr coordinations expected in this sample (4.9% VF Co/Cr). In the bcc $Co_{1-x}Cr_x$ alloy shell, the Co–Co and Co–Cr coordinations will be $8(1-x)$ and $8x$ respectively (assuming random bonding), while the Co–Co coordination in the bcc Co core will be 8. Hence, if the proportion of Co atoms that are alloyed is f, the net Co–Co and Co–Cr nearest neighbour partial coordinations (N_{Co-Co} and N_{Co-Cr} respectively) should be:

$$N_{Co-Co} = 8f(1-x) + 8(1-f)$$

$$N_{Co-Cr} = 8fx$$

The 'comparative' fitting procedure to the Co edge EXAFS data described in section 3.2 indicated that Co atoms were coordinated slightly more by Co than by Cr atoms. This implies that N_{Co-Co} should be slightly greater than 4, and N_{Co-Cr} slightly less than 4 (given that the total nearest neighbour coordination is 8). With $f = 0.68$, this requirement gives us that the Co content in the alloy shell should be greater than 27
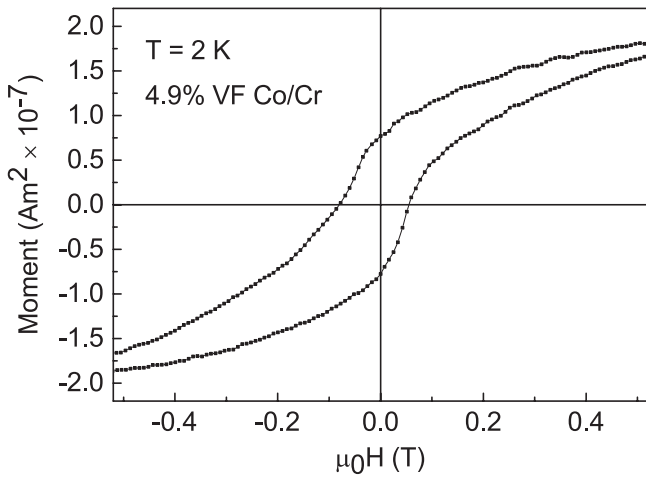
Figure 7. Magnetisation curve (total sample magnetic moment as a function of applied magnetic field) between $\pm 0.5T$ for the 4.9% VF Co/Cr film, measured at a temperature of 2 K after field-cooling at $0.1T$ from room temperature.
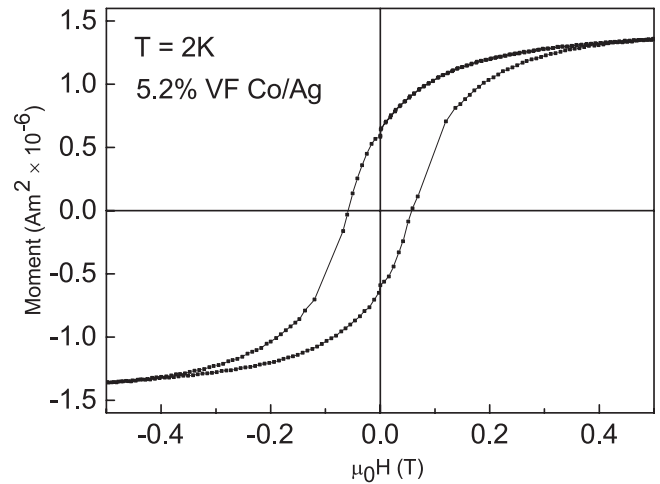

Figure 9. Magnetisation curve (total sample magnetic moment as a function of applied magnetic field) between $\pm 0.5T$ for the 5.2% VF Co/Ag film, measured at a temperature of 2 K after field-cooling at $0.1T$ from room temperature.
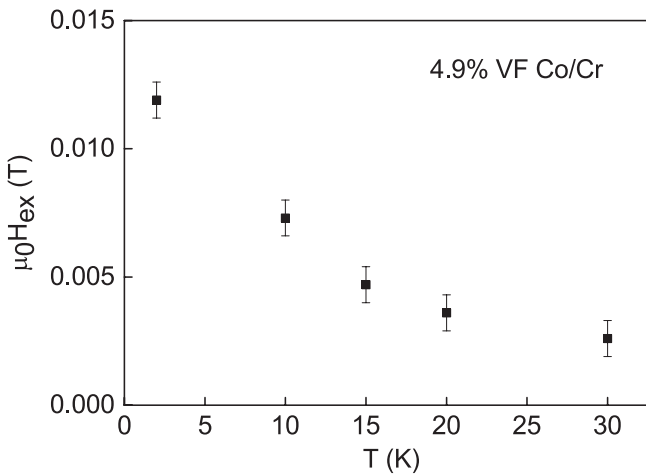

Figure 8. Exchange bias $\mu_0 H$ as a function of temperature for the 4.9% VF Co/Cr film.
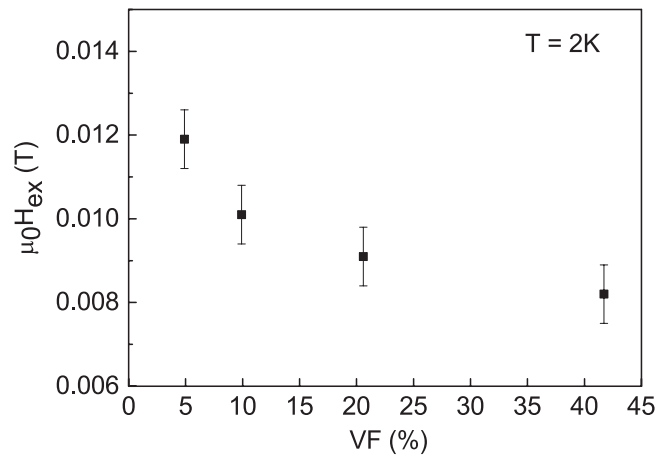

Figure 10. Exchange bias $\mu_0 H$, measured at 2 K after field cooling at $0.1T$ from room temperature, in the nanocomposite Co/Cr films as a function of volume fraction of embedded Co nanoparticles.

at.%. So compositions in the alloy shell which are at the upper end of the composition range reported for bcc $Co_{1-x}Cr_x$ alloys (~30 at.%) [54] are consistent with the Co edge EXAFS.

The formation of a F/AF core/shell structure in the Cr-embedded Co nanoparticles through alloying should result in exchange bias behaviour, due to exchange coupling at the F/AF interfaces in the nanocomposite material. Figure 7 shows the portion of the magnetisation curve (measured at 2 K) between $\pm 0.5T$ for the 4.9% VF Co/Cr sample; a small exchange bias $\mu_0 H_{ex}$ of $0.0119T$ is evident. As can be seen from figure 8, which shows the exchange bias for the above sample as a function of temperature, the exchange bias decreases with increasing temperature and is close to zero for temperatures around 30 K. This is similar to the temperature-dependence of the exchange bias seen in the Mn-embedded Co nanoparticles [36, 37] and Cr-embedded Fe nanoparticles [40]. For comparison, a dilute sample of Co nanoparticles (5.2% VF) in a Ag matrix was prepared. The proportion of the magnetisation curve between $\pm 0.5T$ (at 2 K) for this sample is shown in figure 9; the fact that there is a negligible

exchange bias in this case indicates that Co nanoparticles produced by the source used in our work are not subject to significant oxidation effects, and is consistent with the lack of oxidation related features in the measured Co edge EXAFS (mentioned in section 3.2).

Figures 10 and 11 give the exchange bias and (field-cooled) coercivity $\mu_0 H_c$ (both measured at 2 K) respectively as a function of VF of Co nanoparticles in Cr. For the most dilute concentrations of Co nanoparticles the exchange bias is a significant fraction of the coercivity, with $H_{ex}/H_c \approx 20\%$. The efficiency of the exchange bias effect decreases as the volume fraction of Co nanoparticles is increased, with H_{ex}/H_c falling to ~10% for the highest volume fractions studied. As the fraction of embedded nanoparticles increases from dilute values, where the nanoparticles are effectively isolated from one another, agglomerations of nanoparticles will begin to form in the nanocomposite film. As mentioned earlier, the number of these will become significant as the filling fraction of nanoparticles approaches the percolation threshold of 24.88% [55]. In the film as a whole, agglomeration will serve to reduce the
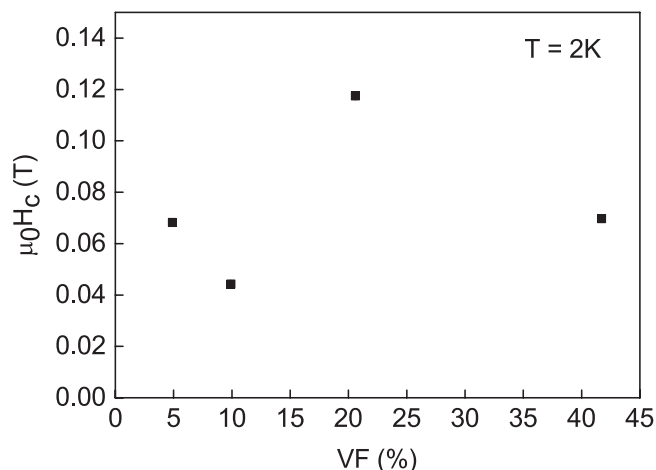
Figure 11. Coercivity $\mu_0 H_c$, measured at 2 K after field cooling at 0.1 *T* from room temperature, in the nanocomposite Co/Cr films as a function of volume fraction of embedded Co nanoparticles.

amount of CoCr alloy shell. The decrease in exchange bias with increasing VF, as shown in figure 10, is therefore consistent with this. In Mn-embedded Co nanoparticles [36, 37], for which there is significant alloying between Co and Mn, H_{ex}/H_c was also found to decrease as the volume fraction of Co nanoparticles increases. In contrast the efficiency of the exchange bias effect in Cr-embedded Fe nanoparticles, where there is not significant alloying, increases as the volume fraction of Fe nanoparticles is increased [40]. In this respect, the similarity between the Cr-embedded and Mn-embedded Co nanoparticles gives further qualitative support for some alloying between Co nanoparticles and Cr matrix.

5. Conclusions

We have investigated atomic structure and magnetism in nanocomposite films of Co nanoparticles embedded in a Cr matrix. The Co nanoparticles adopt the same bcc structure type as the host matrix, although with a degree of disorder. Net atomic moments in the Cr-embedded Co nanoparticles are much reduced compared to the value in bulk Co, with values as low as 0.25 μ_B/atom measured for samples with dilute concentrations of nanoparticles. The structural and magnetic data are both consistent with a degree of alloying at the nanoparticle/matrix interface. This leads to a core/shell structure in the Cr-embedded nanoparticles, with an AF CoCr alloy shell surrounding a reduced Co core.

Acknowledgments

References

[1] Billas I M L, Becker J A, Châtelain A and de Heer W A 1993 *Phys. Rev. Lett.* **71** 4067

[2] Douglass D C, Cox A J, Bucher J P and Bloomfield L A 1993 *Phys. Rev. B* **47** 12874

[3] Baker S H, Binns C, Edmonds K W, Maher M J, Thornton S C, Louch S and Dhesi S S 2002 *J. Magn. Magn. Mater.* **247** 19

[4] Lau J T, Fohlisch A, Nietubye R, Rief M and Wurth W 2002 *Phys. Rev. Lett.* **89** 057201

[5] Bansmann J *et al* 2005 *Surf. Sci. Rep.* **56** 189

[6] Douglass D C, Bucher J P and Bloomfield L A 1992 *Phys. Rev. Lett.* **68** 1774

[7] Cox A J, Louderback J G, Apsel S E and Bloomfield L A 1994 *Phys. Rev. B* **49** 12295

[8] García Prieto A, Fdez-Gubieda M L, García-Arribas A, Barandiarán J M, Meneghini C and Mobilio S 2000 *J. Magn. Magn. Mater.* **221** 80

[9] Vergara M P C, Cezar J C, Tolentino H C N and Knobel M 2002 *Phys. B* **320** 143

[10] Cezar J C, Tolentino H C N and Knobel M 2003 *Phys. Rev. B* **68** 0544041

[11] Jamet M, Dupuis V, Mélinon P, Guiraud G, Pérez A, Wernsdorfer W, Traverse A and Baguenard B 2000 *Phys. Rev. B* **62** 493

[12] Tuaillon J, Dupuis V, Mélinon P, Prével B, Treilleux M, Pérez A, Pellarin M, Vaille J L and Broyer M 1997 *Phil. Mag. A* **76** 493

[13] Dupuis V, Jamet M, Favre L, Tuiallon-Combes J, Mélinon P and Pérez A 2003 *J. Vac. Sci. Technol. A* **21** 1519

[14] Favre L, Stanescu S, Dupuis V, Bernstein E, Epicier T, Mélinon P and Pérez A 2004 *Appl. Surf. Sci.* **226** 265

[15] Baker S H, Roy M, Louch S and Binns C 2006 *J. Phys.: Condens. Matter* **18** 2385

[16] Baker S H, Roy M, Gurman S J, Louch S, Bleloch A and Binns C 2004 *J. Phys.: Condens. Matter* **16** 7813

[17] Sakurai M, Makhlouf S A, Hihara T, Sumiyama K, Wakoh K and Suzuki K 1995 *Phys. B* **208** 614

[18] Baker S H, Asaduzzaman A M, Roy M, Gurman S J, Binns C, Blackman J A and Xie Y 2008 *Phys. Rev. B* **78** 014422

[19] Baker S H, Roy M, Gurman S J and Binns C 2009 *J. Phys.: Condens. Matter* **21** 183002

[20] Baker S H, Roy M, Thornton S C and Binns C 2012 *J. Phys.: Condens. Matter* **24** 176001

[21] Baker S H, Lees M, Roy M and Binns C 2013 *J. Phys.: Condens. Matter* **25** 386004

[22] Pérez A *et al* 1997 *J. Phys. D: Appl. Phys.* **30** 709

[23] Moruzzi V L, Marcus P M, Schwarz K and Mohn P 1986 *Phys. Rev. B* **34** 1784

[24] Guenzburger D and Ellis D E 1995 *Phys. Rev. B* **51** 12519

[25] Moruzzi V L, Marcus P M and Kübler J 1989 *Phys. Rev. B* **39** 6957

[26] Jones N 2011 *Nature* **472** 22

[27] Skumryev V, Stoyanov S, Zhang Y, Hadjipanayis G, Givord D and Nogués J 2003 *Nature* **423** 850

[28] Pankhurst Q A, Thanh N T K, Jones S K and Dobson J 2009 *J. Phys. D: Appl. Phys.* **42** 224001

[29] Thiesen B and Jordan A 2008 *Int. J. Hyperth.* **24** 467

[30] Nogues J, Sort J, Langlais V, Skumryev V, Surinach S, Munoz J S and Baro M D 2005 *Phys. Rep.* **422** 65

[31] Nogués J and Schuller I K 1999 *J. Magn. Magn. Mater.* **192** 203–32

[32] Berkowitz A E and Takano K 1999 *J. Magn. Magn. Mater.* **200** 552–70

[33] Ohldag H, Scholl A, Nolting F, Arenholz E, Maat S, Young A T, Carey M and Stöhr J 2003 *Phys. Rev. Lett.* **91** 017203

[34] Meiklejohn W H and Bean C P 1956 *Phys. Rev.* **102** 1413

[35] Dieny B, Sperious V S, Parkin S S P, Gurney B A, Wilhoit D R and Mauri D 1991 *Phys. Rev. B* **43** 1297

[36] Domingo N, Testa A M, Fiorani D, Binns C, Baker S and Tejada J 2007 *J. Magn. Magn. Mater.* **316** 155–8

[37] Domingo N, Fiorani D, Testa A M, Binns C, Baker S and Tejada J 2008 *J. Phys.* D **41** 134009
[38] Binns C *et al* 2010 *J. Phys.: Condens. Matter* **22** 436005
[39] Laureti S, Peddis D, Del Bianco L, Testa A M, Varvaro G, Agostinelli E, Binns C, Baker S, Qureshi M and Fiorani D 2012 *J. Magn. Magn. Mater.* **324** 3503
[40] Qureshi M T, Baker S H, Binns C, Roy M, Laureti S, Fiorani D and Peddis D 2015 *J. Magn. Magn. Mater.* **378** 345
[41] Sort J, Nogues J, Amils X, Surinach S, Munoz J S and Baro M D 1999 *Appl. Phys. Lett.* **75** 3177
[42] Sort J, Nogues J, Surinach S, Munoz J S, Baro M D, Chappel E, Dupont F and Chouteau G 2001 *Appl. Phys. Lett.* **79** 1142
[43] Stoyanov S, Skumryev V, Zhang Y, Huang Y, Hadjipanayis G C and Nogues J 2003 *J. Appl. Phys.* **93** 7592
[44] Binns C *et al* 2012 *J. Nanopart. Res.* **14** 1136
[45] Binns C *et al* 2005 *J. Phys. D: Appl. Phys.* **38** R357
[46] Baker S H, Thornton S C, Edmonds K W, Maher M J, Norris C and Binns C 2000 *Rev. Sci. Instrum.* **71** 3178
[47] Iles G N, Baker S H, Thornton S C and Binns C 2009 *J. Appl. Phys.* **105** 024306
[48] Tenderholt A, Hedman B and Hodgson K O 2007 *AIP Conf. Proc.* **882** 105
[49] Binsted N 1998 *EXCURV98: Daresbury Laboratory Computer Program*
[50] Gurman S J, Binsted N and Ross I 1984 *J. Phys. C: Solid State Phys.* **17** 143
[51] Roy M and Gurman S J 2001 *J. Synchrotron. Radiat.* **8** 1095
[52] Saib A M, Borgna A, van de Lousdrecht J, van Berge P J and Niemantsverdriet P J 2006 *Appl. Catalysis A: General* **312** 12
[53] Binns C 2010 *Introduction to Nanoscience and Technology* (Hoboken, NJ: Wiley)
[54] Betancourt-Cantera J A, Sanchez-De Jesus F, Bolarin-Miro A M, Betancourt I and Torres-Villasenor G 2014 *J. Magn. Magn. Mater.* **354** 178
[55] Stauffer D and Aharony A 1994 *Introduction to Percolation Theory* (London: Taylor and Francis)
[56] Crangle J 1957 *Phil. Mag.* **2** 659
[57] Bolzoni F, Leccabue F, Panizzieri R and Pareti L 1983 *J. Magn. Magn. Mater.* **31–34** 845
[58] Haines W G 1984 *J. Appl. Phys.* **55** 2263
[59] Chen C W 1977 *Magnetism and Metallurgy of Soft Magnetic Materials* vol XV (Amsterdam: North-Holland) p 184
[60] Asaduzzaman A M and Blackman J A 2010 *Phys. Rev.* B **82** 134417